



## Dynamic modeling and analysis of rolling bearings with rolling element defect considering time-varying impact force

Ruiqi Zhang<sup>b</sup>, Liang Guo<sup>a,b,\*</sup>, Zhuyuxiu Zong<sup>b</sup>, Hongli Gao<sup>b</sup>, Mengui Qian<sup>b</sup>, Zaigang Chen<sup>c</sup>

<sup>a</sup> The State Key Laboratory of Mechanical Transmissions, Chongqing University, Chongqing, China

<sup>b</sup> School of Mechanical Engineering, Southwest Jiaotong University, Chengdu, China

<sup>c</sup> State Key Laboratory of Traction Power, Southwest Jiaotong University, Chengdu, China



### ARTICLE INFO

#### Keywords:

Bearing dynamics  
Rolling element fault  
Fault diagnosis  
Rolling bearing

### ABSTRACT

Accurately establishing a dynamic model of rolling bearings is significant for understanding the fault mechanism and analyzing the motion characteristics under different performance states. Since the contact process of rolling element defect is more complicated than that of race defect, the research on its characteristics is usually simplified to a certain extent. However, the excitation of the rolling element defect area is closely related to the rotational speed and the size of the defect, the commonly used displacement form of fault excitation can hardly reflect the mechanical characteristics of the actual rolling element fault. A time-varying displacement excitation function of the rolling elements is used to characterize the change of the contact gap between the rolling elements and the inner and outer races. According to the time-varying displacement excitation function, a time-varying impact force excitation function of the defective rolling element is proposed which comprehensively considers defect sizes and the rotational speeds. A four-degree-of-freedom bearing dynamics model based on Hertz basis theory is correlated with time-varying excitation, and the accuracy of the model is confirmed by comparison with the processed experimental signal. Based on the mechanical model and experimental data, the influence of the rotational speeds and defect sizes on the vibration characteristics of the bearing rolling element fault is analyzed and summarized, which provides theoretical support for investigating the mechanism of the bearing rolling element fault.

### 1. Introduction

Rolling bearings are widely used in different types of rotating machines, and their performance directly determines the operating quality of the mechanical equipment [1–4]. The local defects of bearings will quickly degrade their performance. Therefore, the fault diagnosis research of bearings is significant. Many effective fault diagnosis methods have been widely used in the development of the past ten years [5–9]. In order to have a more in-depth understanding of the evolution process and fault characteristics of bearing defects, the establishment of corresponding physical models to study its vibration characteristics has become a reliable theoretical basis of fault diagnosis [10–12].

The classical physical models of bearings use shock sequences to characterize vibrations. McFadden and Smith [13,14] proposed a

\* Corresponding author.

E-mail address: [guoliang@swjtu.edu.cn](mailto:guoliang@swjtu.edu.cn) (L. Guo).

bearing vibration model for inner race fault. The model used a periodic pulse function to express the rotation of the bearing, and multiplied the pulse function with the load distribution function, transfer function, and exponential decay function. This method laid the foundation for the method of simulating vibration signals using shock sequences. Antoni and Randall [15,16] considered the random sliding of rolling elements and cages, and perfected it into a pseudo-cyclic stationary signal model. Tandon and Choudhury [17] investigated the influence of different defect forms on analog signals. It was difficult to use shock sequence to simulate vibration signals to reveal the overall contribution of bearing single components to vibration. Therefore, some efficient and intuitive approaches have been proposed to investigate the vibration characteristics of bearings.

Feng et al. [18] modeled the bearing system as a four-degree-of-freedom system consisting of a rotor concentrated mass block, a base concentrated mass block and spring damping. Based on Feng's four-degree-of-freedom model, Sawalhi and Randall [19,20] added a small spring damping with a higher damping coefficient in the vertical direction to simulate the typical high-frequency resonance response of the bearing. Petersen et al. [21] proposed a dynamic model for double-row bearings. A spring-damping-mass block was added in the horizontal and radial directions to simulate the high-frequency resonance response. Niu et al. [22] modeled the shape of the outer raceway defect as a circle, which considered the influence of factors such as gyro torque, centrifugal force, and slip on the contact force in the case of high-speed motion. Liu et al. [23] investigated the contact mechanics characteristics between the ball with different defect sizes and the race by using the segmented function of excitation in the faulty interval. Kulkarni and Sahasrabudhe [24] used cubic spline interpolation curve as the displacement excitation when the rolling element passed the outer race defect, and investigated the influence of the defect size and the location on the simulation results. Jiang et al. [25] considered the contact relationship between the rolling elements and the defect area in the three-dimensional space for the local defects of the outer raceway, and deduced the motion trajectory closer to the actual behavior of the rolling element. The proposed model investigated the influence of different size defects in the axial and radial directions on the contact force and vibration signals. In order to reveal the slip characteristics of rolling bearings, Liu et al. [26] discretized the cage into several segments with the same number of rolling elements. Liu investigated the effects of time-varying contact stiffness and edge topography of defects in ball bearings with raceway defects [27–29]. Shah and Patel [30] considered the geometric dimensions of the local defects of the rolling bearing race and the rotational speed, and proposed a dynamic model under time-varying excitation. Some scholars had investigated the impact process of race fault in bearings. Khanam et al. [31] investigated the impact force under outer race fault based on the engineering mechanics approach and obtained the response of deep groove ball bearings with different defect sizes and different rotational speed. Liu and Guo [32] investigated the impact force under outer race fault by impulse theorem, but the specific derivation of some key parameters and the frequency domain analysis of the experimental results were not given. Sassi et al. [33] used the kinetic energy of the system to derive the excitation function when the rolling elements were in the defect area, and proposed a three-degree-of-freedom dynamic model of bearings.

In the above research, most of the research topics are the race defects that occur in the inner and outer races of bearings. Compared with race faults, rolling element faults have more complex contact characteristics [34]. Many researchers have investigated the mechanism of rolling element faults. Mishra et al. [35] proposed a plane motion model including cage, traction and contact dynamics in the form of a multi-energy domain bond graph in the Symbols software. Cao and Xiao [36] carried out comprehensive modeling work for spherical roller bearings. In addition to the vertical and horizontal displacements considered in previous studies, the influence of axial displacement and load was considered by introducing degrees of freedom in the axial direction. Choudhury and Tandon [37] proposed a theoretical model of the vibration response of local defects of each bearing element of the rotor-bearing system under radial load. Arslan and Aktürk [38] proposed a shaft-bearing model to investigate the vibration of the rolling parts of defective and non-defective angular contact ball bearings. Rafsanjani et al. [39] proposed a non-linear dynamic model with local defects of rolling elements and races, which used an improved Newmark time integration method to numerically solve the equations of motion. Gupta [40,41] proposed a relatively complete high-degree-of-freedom dynamic model based on the relative positional relationship between various components. On the basis of the model proposed by Gupta, Cao et al. [42] proposed a dynamic model of the local defect vibration of cylindrical roller bearings, which was used to investigate the vibration response of single defect, multiple defects and composite defects. Niu et al. [43] proposed a dynamic model of cylindrical roller bearings with roller defects, which was used to investigate the vibration response of the bearing when the roller defects bypassed outer races and inner races.

To sum up, some scholars have done systematic research on rolling elements. However, the excitation force is usually simplified and the time-varying characteristics of the contact process are not fully investigated in these studies. At the same time, when the same defect occurs in different experimental equipment, the signal characteristics in the frequency domain are obviously different. The signal characteristics are also significantly different under different working conditions in the same data set. Because of the weak generalization ability of the classic single displacement excitation fault model, it cannot reflect the true vibration characteristics of the data. In response to the above problems, a displacement excitation function reflecting the rolling characteristics of the rolling elements is proposed in this paper. On this basis, a time-varying impact force excitation function of the defective rolling element is derived which comprehensively considers the size of the defect and the rotational speed of the bearing. The two excitation functions include the influence of factors such as the size of the rolling element defect and the rotational speed. They can reflect the contact process of the rolling element defect area more soundly. Furthermore, this function is introduced into a four-degree-of-freedom dynamic model based on the Hertz contact theory to obtain simulated signals. Based on the wavelet packet signal processing method, the simulated signal generated by this model and actual data are used to analyze the mechanism of the rolling element fault. The experimental results reveal the model is self-consistent.

## 2. Time-varying excitation model of the defective rolling element

When there is a local defect in the rolling elements of a rolling bearing, the rotation of rolling elements and the revolution with the

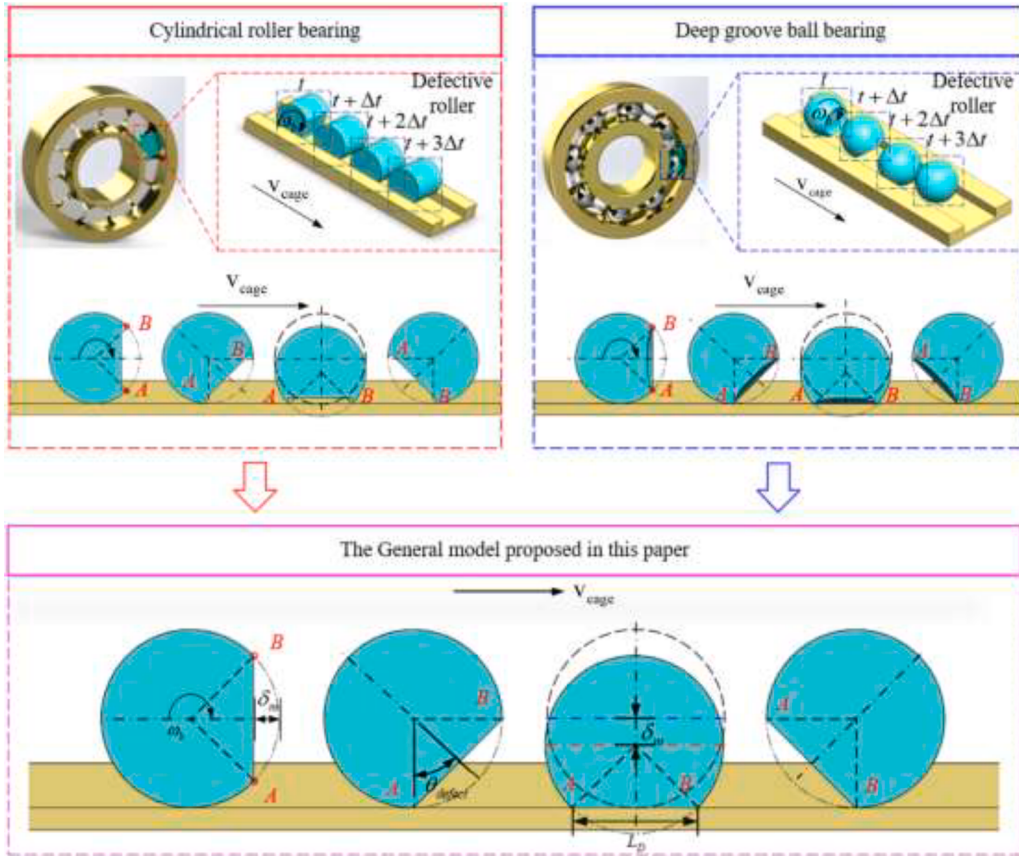


**Fig. 1.** Simplification of the movement process of the defective rolling element.

cage cause the local defect to alternately contact its inner and outer races. Defective rolling elements will produce additional displacement, hence making the bearing produce extra excitation force. This is the cause of the abnormal vibration components of a defective bearing. The components have a trend relationship with defect sizes and rotational speeds. The relationship will be discussed and analyzed in the following chapters. This chapter proposes a displacement excitation model, and derives the time-varying excitation function of the impact force according to the displacement excitation function.

The dynamic models presented in this paper are based on the following assumptions:

- The movement of the bearing is limited to the radial plane of the bearing;
- The contact form between the rolling element and the inner and outer races of the bearing is Hertz contact, and the contact between the rolling elements and the cage does not generate additional force;
- There is no relative sliding between the inner race and the shaft. The angular velocity of the inner race is the same as the rotational speed of the shaft;
- The position of the center of mass of the rolling element is always maintained at the geometric center;
- The damage form of the bearing is assumed to be a regular plane related to the width of the defect.

## 2.1. Dynamic model of the rolling elements

It is crucial to investigate the rotation and revolution process of defective rolling elements. The investigation into the rolling elements with local defects needs to be based on the simplified objects of their complex geometric structures. The geometric model of the bearing used in this paper is shown in Fig. 1. The colored rolling element is a rolling element with a local defect.

The motion state of rolling elements includes the self-rotation around its center of mass and the revolution with the cage. A bearing is expanded along the rotation direction of the cage in Fig. 1. The process of rotating around the axis is abstracted as a linear motion process, which plays an important role in the discussion of the subsequent motion state of rolling elements.

When a rolling element does not slip, the rotational speed  $\omega_b$  can be calculated by the fault frequency of the rolling element [44], which can be calculated as:

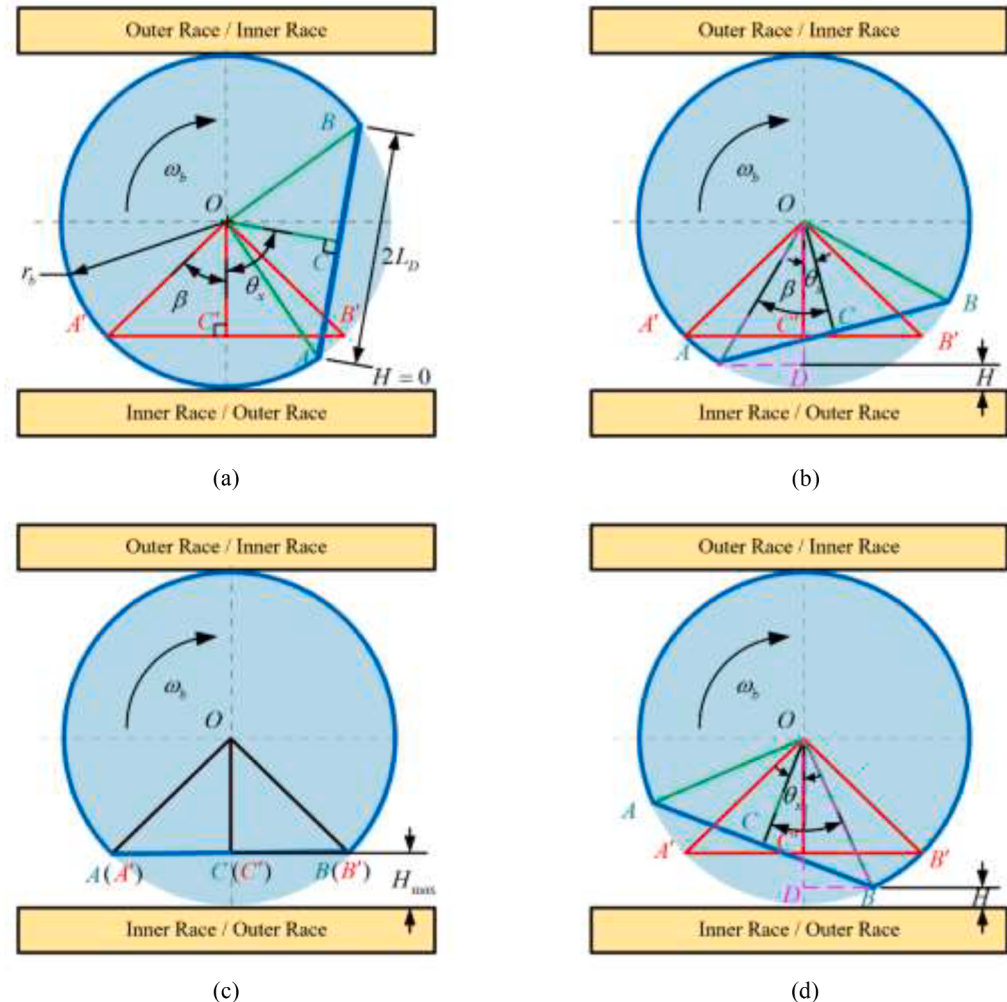


**Fig. 2.** Motion of a defective rolling element on race. (a) Stage1, (b) Stage 2, (c) Stage 3, and (d) Stage 4.

$$\omega_b = \frac{D}{2d} \left[ 1 - \left( \frac{d}{D} \cos \alpha \right)^2 \right] \omega \quad (1)$$

where  $D$  is the pitch diameter;  $d$  is the diameter of rolling elements;  $\alpha$  is the contact angle of rolling elements; and  $\omega$  is the rotational speed.

In addition to the rotation of rolling elements, the angular velocity of cage  $\omega_c$  is calculated as [41]:

$$\omega_c = \frac{1}{2} \left( 1 - \frac{d}{D} \cos \alpha \right) \omega \quad (2)$$

At the time  $t$ , the angular position of the  $j$ -th rolling element can be calculated by the following equation [44]:

$$\varphi_j = (j-1) \frac{2\pi}{N} + \omega_c t \quad (3)$$

where  $N$  is the number of rolling elements.

This paper divides the movement process of rolling elements going through the defect area into four stages. In order to describe its movement process, Fig. 1 shows these states of rolling elements at the same time interval  $\Delta t$ . At the time  $t$ , the rolling element defect does not contact the inner and outer races of the bearing; at the time  $t + \Delta t$ , the front edge of the rolling element partial defect contacts the race for the first time in the cycle of one revolution, and the defective rolling element begins to enter a state where the radial displacement changed; at the time  $t + 2\Delta t$ , the two defective edges A/B of the rolling element are in contact with the race at the same time. In this state, the defective rolling element has the largest radial displacement based on the faulty geometry relative to the inner and outer races; at the time  $t + 3\Delta t$ , the rear edge B of the defective rolling element is in contact with the race. In this state, the

defective rolling element exits the state where the radial displacement changes. It has the same regular contact with the other race.

## 2.2. Displacement excitation function

The formula derivation process of the displacement excitation function can be analyzed in the aforementioned four stages. In order to quantify the time-varying characteristics of the defective rolling element, the red border area in Fig. 2 is the corner position edge of the defect. The length of the line between two points is denoted as  $L_{xx}$ , i.e., the length between point A and point B is denoted as  $L_{AB}$ . The span of this area is calculated as:

$$\beta = \arcsin \frac{L_D}{r_b} \quad (4)$$

where  $L_D$  is half of the width of the rolling element defect;  $r_b$  is the radius of rolling elements.

In Stage1, the defect area is not in contact with the inner and outer races. As shown in Fig. 2, this process is represented as the vertical foot of  $\Delta OAB$  does not enter the fan-shaped defect area formed by the red borders  $OA'$  and  $OB'$ .

In Stage2, the line connecting the center of the defect area and the center of mass is in the first half of the faulty angle interval. The defective rolling element gradually reaches its maximum contact deformation with rotation (Stage 3). During this process,  $OC$  has always been in the fan-shaped area formed by  $OC'$  and  $OB'$ . The angle between  $OC$  and  $OC'$  is defined as  $\theta_x$ , which is calculated as follows:

$$\theta_x = \begin{cases} \text{mod}(\theta_d, 2\pi) - 2\pi, & \text{mod}(\theta_d, 2\pi) > 1.5\pi \\ \text{mod}(\theta_d, 2\pi), & \text{otherwise} \end{cases} \quad (5)$$

where  $\theta_d = \omega_b t$  is the relative position angle of the defective rolling element at time  $t$ .

According to its geometric characteristics, the displacement excitation function at this stage can be deduced as:

$$H = r_b - L_{OD} = r_b - r_b \cos(\beta - |\theta_x|) \quad (6)$$

In Stage3, the line connecting the center of the defect area and the center of mass is perpendicular to the races.  $OC$  and  $OC'$  are completely coincident, and the maximum displacement  $H_{\max}$  is calculated by the following equation:

$$H_{\max} = r_b - r_b \cos \beta \quad (7)$$

In Stage4, the line connecting the center of the defect area and the center of mass is in the second half of the faulty angle interval. During this process,  $OC$  has always been in the fan-shaped area formed by  $OC'$  and  $OA'$ . The calculation of displacement excitation function in Stage4 is the same as that of Stage2. After synthesizing the four stages of motion and considering the alternating effects of the rolling elements and the inner and outer races, the final displacement excitation function is as follows:

$$H = \begin{cases} r_b - r_b \cos(\beta - |\theta_x|), & |\theta_x| < \beta \\ r_b - r_b \cos(\beta - |\theta_x - \pi|), & -\beta + \pi < \theta_x < \beta + \pi \\ 0, & \text{otherwise} \end{cases} \quad (8)$$

## 2.3. Impact force excitation function - Part 1

In classic dynamic models, the displacement excitation function is positively correlated with the contact force, and the faulty impact is simulated by the change of the contact force. The sudden change in clearance reflects the effect of the bearing defect area to some extent. However, the interaction effect between the defect edge and the race is not considered. The existing methods of impact force are different, and most of the research objects are the defects of inner and outer races [45,46]. Based on the velocity variation of the contact point, the impact force excitation function when a defect is located on the rolling element is derived in this section.

The faulty form of rolling elements is difficult to predict. Unlike the race fault, the rotation motion of the rolling elements makes the time-varying characteristics of the faulty position more complicated, which leads to an extremely challenging task to accurately derive the impact force.

During the movement of the defective rolling element, the tangential velocity  $V_c$  (the tangential direction refers to the tangential direction of the rolling element in the radial plane with respect to the direction of rotation) characterizes its tangential motion state. Due to the constant speed of the rolling element's rotation, the value of  $V_c$  is constant here. The radial velocity  $V$  characterizes its tangential motion state. The change of  $V$  causes the change of the tangential acceleration, which is finally manifested as the tangential component of the impact force.

When the scaling factor is not taken into consideration, the displacement changes of the inner race and the outer race are the same. Therefore, the situation of  $|\theta_x| < \beta$  is taken to discuss. The displacement excitation function has been obtained in the previous chapters. Rewrite it as a piecewise function of the following form:

$$H = \begin{cases} r_b - r_b \cos(\beta + \theta_x), & -\beta \leq \theta_x \leq 0 \\ r_b - r_b \cos(\beta - \theta_x), & 0 < \theta_x \leq \beta \end{cases} \quad (9)$$

Through the displacement piecewise function in Eq. (9), the radial velocity can be obtained as follows:

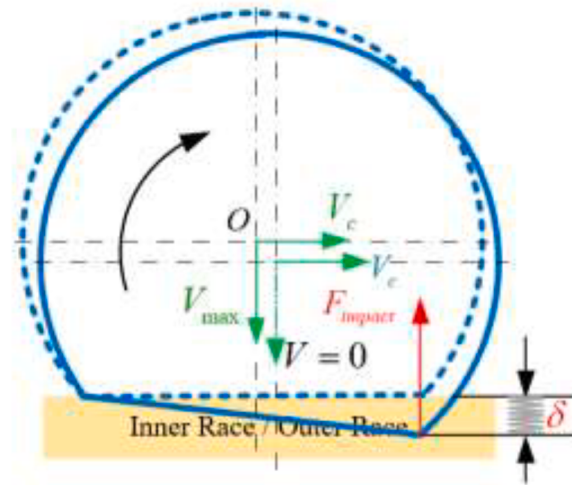


**Fig. 3.** Definition of impact force at contact point.

$$V = \frac{dH}{dt} = \begin{cases} r_b \times \omega_b \times \sin(\beta + \theta_x), -\beta \leq \theta_x \leq 0 \\ -r_b \times \omega_b \times \sin(\beta - \theta_x), 0 < \theta_x \leq \beta \end{cases} \quad (10)$$

It can be deduced that at the moment  $\theta_x = 0$ , the velocity reaches its maximum, defined as  $V_{\max}$ . The direction of  $V_{\max}$  instant changes to the reverse, and according to the conservation of energy, the velocity change is accompanied by the impact phenomenon. The impact force caused instantaneously by the impact can be obtained by the elastic deformation of the contact position [31]. The definition of the impact process in this paper is shown in Fig. 3.

The potential energy of the elastic deformation at the contact position is:

$$P = \int_0^\delta k_c x^n dx = \frac{1}{n+1} k_c \delta^{n+1} \quad (11)$$

where  $k_c$  is the contact stiffness;  $n$  is the loaddeflection exponent;  $\delta$  is the maximum contact deformation.

The change in kinetic energy before and after contact is shown below:

$$K = \frac{1}{2} m_b V_{\max}^2 - 0 = \frac{m_b r_b^2 \omega_b^2 \sin^2 \beta}{2} \quad (12)$$

According to the conservation of energy, the maximum contact deformation is as follows:

$$\delta = \left( \frac{(n+1)m_b r_b^2 \omega_b^2 \sin^2 \beta}{2k_c} \right)^{\frac{1}{n+1}} \quad (13)$$

The maximum contact force (impact force) is as follows:

$$F_c|_{\max} = k_c \delta^n = k_c \cdot \left( \frac{(n+1)m_b r_b^2 \omega_b^2 \sin^2 \beta}{2k_c} \right)^{\frac{n}{n+1}} = k_c^{\frac{1}{n+1}} \left( \frac{(n+1)}{2} m_b r_b^2 \omega_b^2 \sin^2 \beta \right)^{\frac{n}{n+1}} \quad (14)$$

Considering the deformation process of the maximum contact force, the expression of the impact force is as follows:

$$F_{\text{impact}} = \begin{cases} F_c|_{\max} \left( \frac{\delta - (H_{\max} - H)}{\delta} \right)^{\frac{n}{n+1}}, & H_{\max} - \delta \leq H \leq H_{\max} \\ 0, & \text{otherwise} \end{cases} \quad (15)$$

Assuming a defective rolling element numbered  $d$ , the derivation of  $F_{\text{impact}}$  is as follows:

$$F_{imx-1} = \begin{cases} F_{\text{impact}} \sin \varphi_d, & \theta_x \in [-\beta, \beta] \\ -F_{\text{impact}} \sin \varphi_d, & \theta_x \in [-\beta + \pi, \beta + \pi] \\ 0, & \text{otherwise} \end{cases} \quad (16)$$

$$F_{imy-1} = \begin{cases} F_{\text{impact}} \cos \varphi_d, & \theta_x \in [-\beta, \beta] \\ -F_{\text{impact}} \cos \varphi_d, & \theta_x \in [-\beta + \pi, \beta + \pi] \\ 0, & \text{otherwise} \end{cases} \quad (17)$$

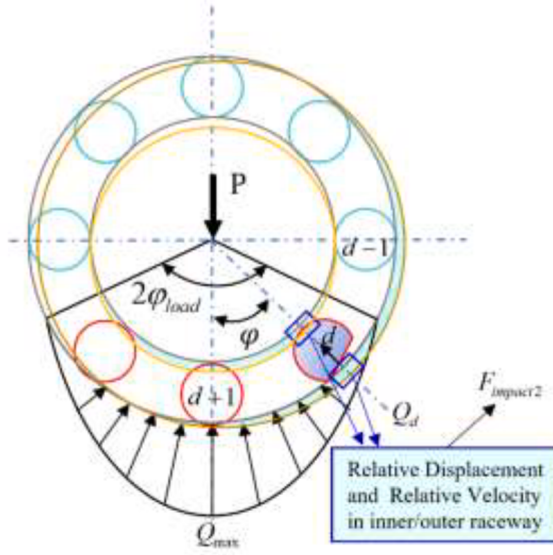


**Fig. 4.** Load distribution in the bearing.

#### 2.4. Impact force excitation function - Part 2

In Part 1, the additional impact force of the defective rolling element is deduced. However, when the bearing is subjected to radial load, the rolling elements in the load zone are squeezed and radial load is generated. Due to the presence of the extrusion load, the additional impact force of the defective rolling element in the load zone  $F_{\text{impact}2}$  is considered.

The load distribution of a rolling bearing under the radial force is showed in Fig. 4. The rolling element, whose center is collinear with the external force, bears the maximal component force. With angular position changing, the load is gradually reduced until it is decreased to zero at the boundary of load zone. Within the load zone, the normal load on the rolling element/races is provided by the following expression:

$$Q_d = \begin{cases} Q_{\max} \left[ 1 - \frac{1}{2\varepsilon} (1 - \cos\varphi) \right]^n, & \varphi \in \varphi_{\text{load}} \\ 0, & \varphi \notin \varphi_{\text{load}} \end{cases} \quad (18)$$

where  $\varphi$  is the angle measured from the maximum load direction;  $\varphi_{\text{load}}$  is the angular limit of the load zone;  $Q_{\max}$  is the maximum rolling load and  $\varepsilon$  is the load distribution factor given by  $\varepsilon = (1/2)(1 - C_r/2\delta_r)$ ; where  $C_r$  is the diametric clearance and  $\delta_r$  is the radial shift of the race at  $\varphi = 0$ .

Although defective rolling elements in the load zone has been exerted by radial loads, the accuracy of their impact forces deduced using the load zone distribution in a healthy state is difficult to guarantee. Accordingly, relative displacement and relative velocity are used for a concise characterization of the impact force. Assuming a defective rolling element numbered  $d$ , the derivation of  $F_{\text{impact}2}$  in the load zone is as follows:

$$\begin{aligned} F_{\text{impact}2} &= \frac{m_b \Delta v / \Delta t}{m_b (\Delta \delta)' / \Delta t} \\ &= m_b [(\Delta x \sin \varphi_d + \Delta y \cos \varphi_d - C_r)|_{t=0+\Delta t} - (\Delta x \sin \varphi_d + \Delta y \cos \varphi_d - C_r)|_{t=0}]' / \Delta t \\ &= m_b [(\Delta x|_{t=0+\Delta t} - \Delta x|_{t=0}) \sin \varphi_d + (\Delta y|_{t=0+\Delta t} - \Delta y|_{t=0}) \cos \varphi_d] / \Delta t \\ &= m_b [(\Delta x|_{t=0+\Delta t} - \Delta x|_{t=0}) \sin \varphi_d + (\Delta y|_{t=0+\Delta t} - \Delta y|_{t=0}) \cos \varphi_d + \\ &\quad \omega (\Delta x'|_{t=0+\Delta t} - \Delta x'|_{t=0}) \cos \varphi_d - \omega (\Delta y'|_{t=0+\Delta t} - \Delta y'|_{t=0}) \sin \varphi_d] / \Delta t \end{aligned} \quad (19)$$

where  $\Delta v$  and  $\Delta \delta$  are the radial velocity and radial displacement of the defective rolling element, respectively;  $\Delta x$  and  $\Delta y$  are the relative displacements of the inner and outer races in the X and Y directions, respectively;  $\Delta x'$  and  $\Delta y'$  are the relative velocities of the inner and outer races in the X and Y directions, respectively.

It is worth noting that in order to ensure the computational accuracy,  $\Delta t$  should be chosen as small as possible without affecting the computational speed. In this paper, the value is taken as the reciprocal of the sampling frequency.

In summary, the decomposition of the impact force triggered by the external load takes the form shown in Eq. (20) (21):

$$F_{\text{imx-2}} = \begin{cases} F_{\text{impact}2} \sin \varphi_d, & \varphi_d \in \varphi_{\text{load}} \\ 0, & \text{otherwise} \end{cases} \quad (20)$$

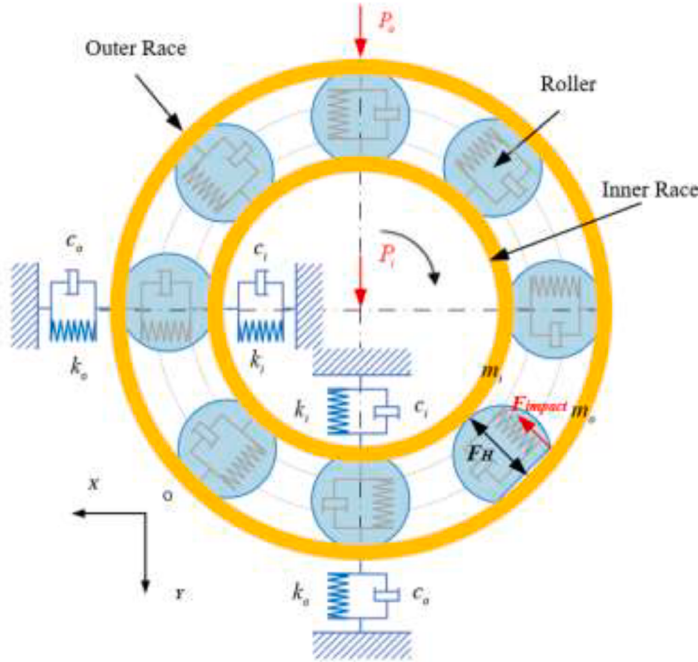


**Fig. 5.** Simplified model of the rolling bearing.

$$F_{imy-2} = \begin{cases} F_{impact2} \cos \varphi_d, & \varphi_d \in \varphi_{load} \\ 0, & \text{otherwise} \end{cases} \quad (21)$$

### 3. Dynamic model of the bearing with rolling element defect

There is a radial clearance between rolling elements and races of rolling bearings. Under the action of radial load, the inner and outer races begin to move and further squeeze the rolling elements to produce elastic deformation. When the defects contact races, additional displacement is generated in the radial direction, resulting in a decrease in elastic deformation. The displacement excitation function of the defect area is equivalent to the change of the clearance. The radial elastic deformation  $\delta_j$  of the  $j$ -th rolling element is expressed as:

$$\delta_j = (x_i - x_o) \sin \varphi_j + (y_i - y_o) \cos \varphi_j - C_r - H_j \quad (22)$$

where  $x_i$  and  $x_o$  are the horizontal displacements of the inner and outer races, respectively;  $y_i$  and  $y_o$  are the vertical displacements of the inner and outer races, respectively.  $C_r$  is the radial clearance.  $H_j$  is the additional displacement caused by the defect, Eq. (8) is used to calculate it. In other cases,  $H_j = 0$ .

The Hertz contact force is calculated as follows:

$$\begin{cases} F_{Hx} = K \sum_{j=1}^N \gamma_j \delta_j^n \sin \varphi_j \\ F_{Hy} = K \sum_{j=1}^N \gamma_j \delta_j^n \cos \varphi_j \end{cases} \quad (23)$$

where  $N$  is the number of rolling elements.  $K$  is the equivalent contact stiffness. According to the Hertzian contact theory, the total load-deflection constant between the rolling elements and the races can be calculated by Eq. (24):

$$K = \frac{1}{[(1/K_i)^{1/n} + (1/K_o)^{1/n}]^n} \quad (24)$$

where  $K_i$  and  $K_o$  are the contact stiffness between the rolling element and the inner and outer races, respectively;  $n$  is the loaddeflection exponent,  $n = 3/2$  for ball bearings and  $n = 10/9$  for roller bearings. The contact stiffness  $K_i$  and  $K_o$  can be calculated by Ref. [47].  $\gamma_j$  in Eq. (23) is as follows:

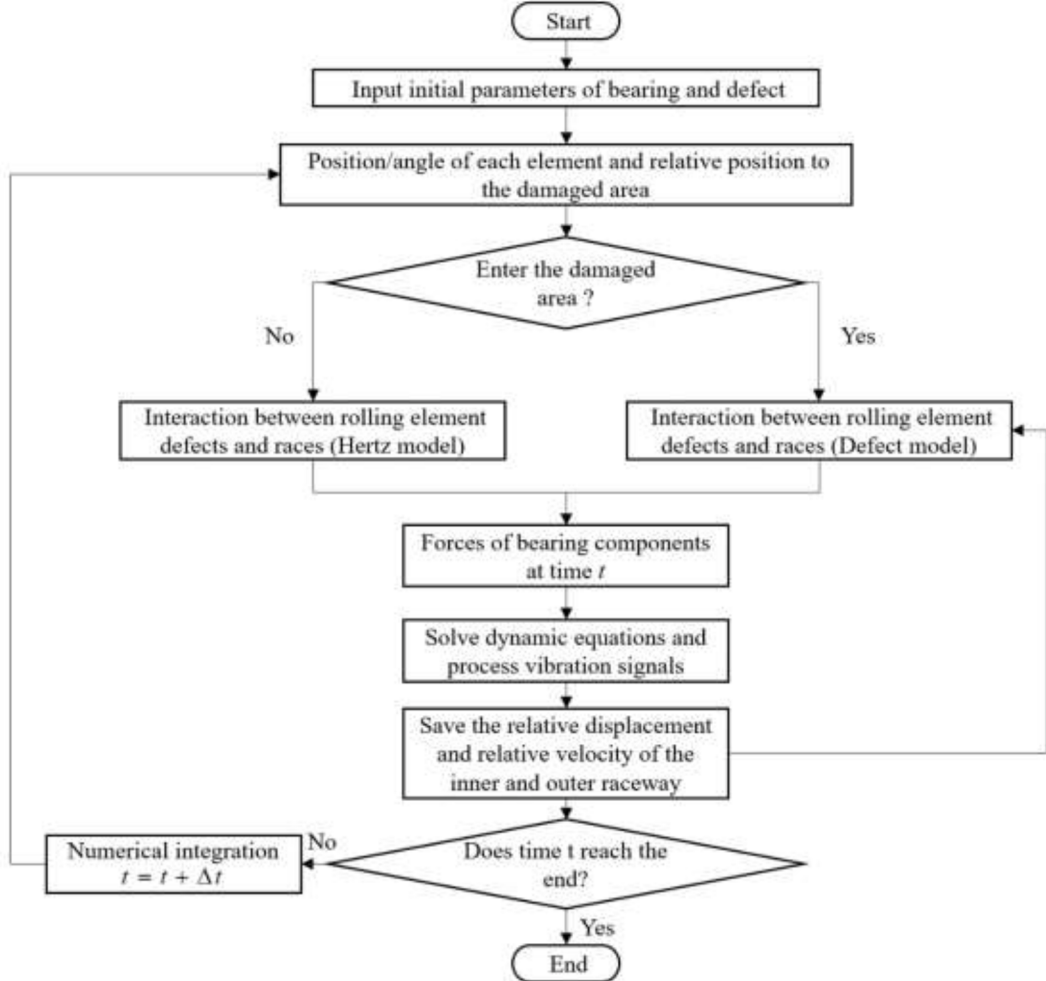


**Fig. 6.** Flowchart of the dynamic simulation.

$$\gamma_j = \begin{cases} 1 & , \delta_j > 0 \\ 0 & , \text{otherwise} \end{cases} \quad (25)$$

Considering the elastohydrodynamic lubrication (EHL), the contact surface of the rolling elements and the races is covered with a lubricating oil film. When the rolling element is squeezed, it has a damping effect on the relative movement of the inner and outer races. After the lubricating action has been suitably simplified [25], the calculation of this force is shown in Eq. (26):

$$\begin{cases} F_{cx} = \sum_{j=1}^N \gamma_j c_b [(\dot{x}_i - \dot{x}_o) \sin \varphi_j + (\dot{y}_i - \dot{y}_o) \cos \varphi_j] \sin \varphi_j \\ F_{cy} = \sum_{j=1}^N \gamma_j c_b [(\dot{x}_i - \dot{x}_o) \sin \varphi_j + (\dot{y}_i - \dot{y}_o) \cos \varphi_j] \cos \varphi_j \end{cases} \quad (26)$$

where  $c_b$  is the viscous damping coefficient.

The dynamic model of rolling bearings in this paper is shown in Fig. 5. Where  $F_H$  represents the contact internal force between the rolling elements and the inner and outer races. When the defect contacts the races, the additional displacement makes it have time-varying characteristics. Assuming that the outer race is fixed, the external radial load is applied to the bearing through the center of the rotating shaft, and further applied to the simplified spring damping system in the vertical direction. The solution equation of the bearing model can be written as:

**Table 1**  
Bearing parameters used in simulation.

Parameters	Value
Radial clearance $C_r$ ( $\mu\text{m}$ )	1
Stiffness of inner race $k_i$ (N/m)	$7.42 \times 10^7$
Stiffness of outer race $k_o$ (N/m)	$1.51 \times 10^7$
Damping coefficient of inner race $c_i$ (Ns/m)	1376
Damping coefficient of outer race $c_o$ (Ns/m)	2210
Eccentricity distance $e$ ( $\mu\text{m}$ )	1
Viscous damping coefficient $c_b$ (Ns/m)	1500

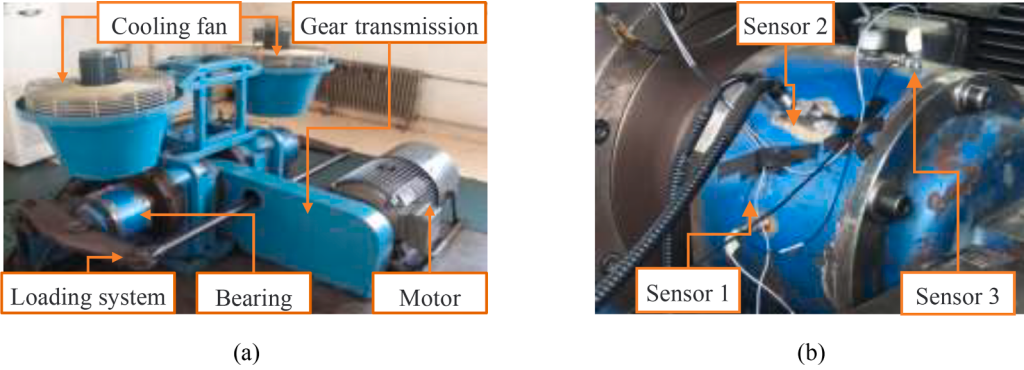


**Fig. 7.** (a) Test rig of Rail Transit Simulation Experiment; (b) Installation of sensors.

$$\begin{cases} m_o \ddot{x}_o + c_o \dot{x}_o + k_o x_o = F_{hx} + F_{cx} + F_{imx-1} + F_{imx-2} \\ m_i \ddot{x}_i + c_i \dot{x}_i + k_i x_i = -F_{hx} - F_{cx} + em_i \omega^2 \cos \omega t + F_{imx-1} - F_{imx-2} \\ m_o \ddot{y}_o + c_o \dot{y}_o + k_o y_o = P_o + F_{hy} + F_{cy} + m_o g + F_{imy-1} + F_{imy-2} \\ m_i \ddot{y}_i + c_i \dot{y}_i + k_i y_i = P_i + m_i g - F_{hy} - F_{cy} + em_i \omega^2 \sin \omega t + F_{imy-1} - F_{imy-2} \end{cases} \quad (27)$$

where  $m_i$  and  $m_o$  are the equivalent masses of the inner and outer races;  $k_i$  and  $k_o$  are the equivalent stiffness at the bearing rotor and base;  $c_i$  and  $c_o$  are the equivalent damping at the bearing rotor and base.  $e$  is the eccentricity.  $P_i$  and  $P_o$  are the externally loaded radial force.

Because of the strong nonlinearity of the dynamic system, the fourth-order Runge-Kutta method is used to solve Eq. (27). The flowchart of the algorithm used in this paper is shown in Fig. 6. The main parameters used in simulation are shown in Table 1.

#### 4. Result and discussion

In order to verify the accuracy and generalization ability of the proposed model, two completely unrelated experimental datasets of bearings are used in this section. Among them, the public dataset from Case Western Reserve University (CWRU dataset) [48] is used to validate the basic performance of the proposed model and the effect of bearing faulty dimensions on the experimental results. The generalization capability of the proposed model and the effect of rotational speed on the experimental results are validated by Rail Transit Simulation Experiment (RTSE dataset).

The stiffness and damping parameters in Table 1 are chosen for both sets of experiments in simulation.

##### 4.1. Dataset description

- 1) CWRU Bearing Data Set: The CWRU rolling bearing dataset is provided by Case Reserve University. The test rig consists of an induction motor, a torque transducer/encoder center, a dynamometer, and control electronics. The signals are collected from the drive end of the motor via a triaxial accelerometer. Electric sparking is applied to process different artificial defect sizes in different positions of bearings. Each faulty condition also contains three faulty severities: 0.1778, 0.3556, 0.5334 mm. Tests are performed under four operating conditions with different motor loads and rotational speeds, i.e., 0 HP/1797 RPM, 1 HP/1772 RPM, 2 HP/1750 RPM and 3 HP/1730 RPM. The sampling frequency is set to 12 kHz for all tests.
- 2) Rail Transit Simulation Experiment Data Set: The experimental bearings are provided by CRRC Qingdao Sifang Rolling Stock Research Institute, which are cylindrical roller bearings. The experimental setup includes a drive motor, a loading system, a cooling system, a gear transmission system and three sensors. The vibration signals are collected by three acceleration sensors arranged on

**Table 2**  
Geometric parameters of the tested bearings.

Parameters	CWRU Deep groove ball bearing	RTSE Cylindrical roller bearing
Type		
Inner race dimension (mm)	17	130
Outer race dimension (mm)	40	230
Pitch dimension (mm)	28.5	180
Roller diameter (mm)	6.746	23.78
Number of rollers	8	20
Contact angle (°)	0	0

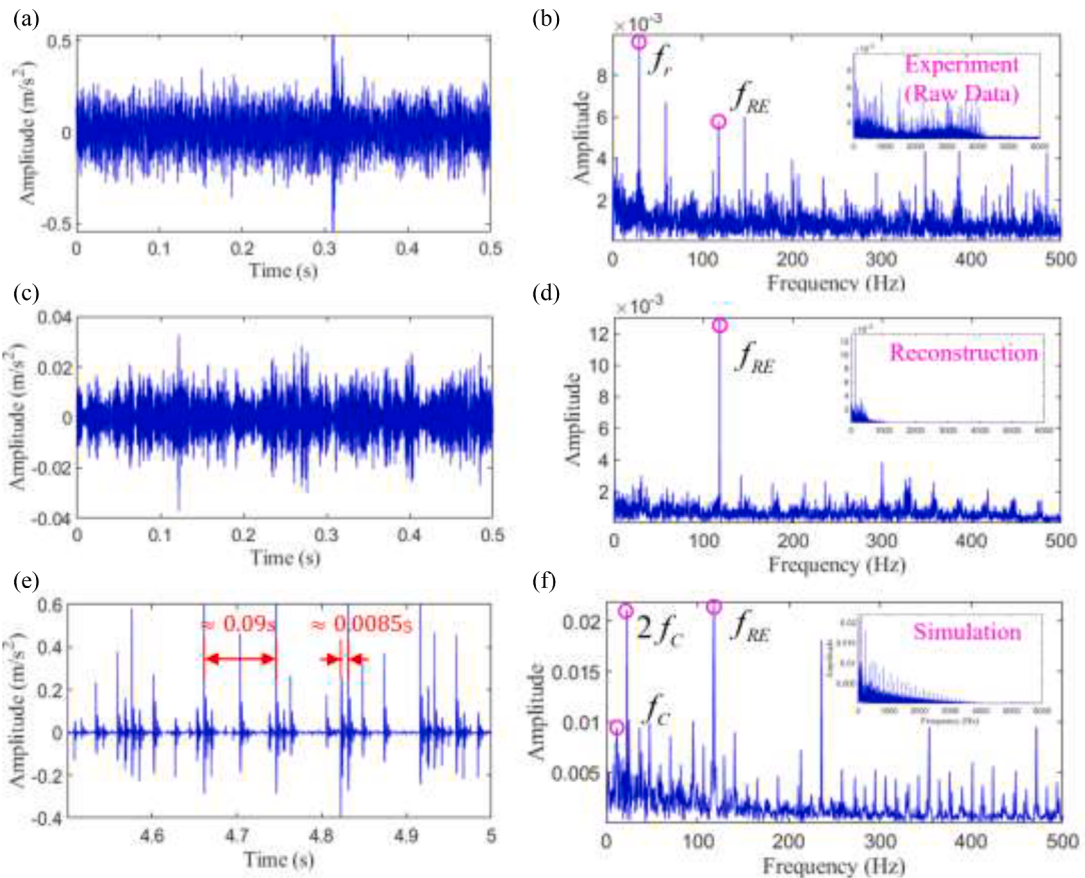


**Fig. 8.** Experiment and simulation results. (a) Time domain signal of the experiment, (b) envelope spectrum (the envelope signal is obtained based on Hilbert transform) of the experiment signal, (c) time domain signal of the reconstructed signal, (d) envelope spectrum of the reconstructed signal, (e) time domain signal of the simulation result, and (f) envelope spectrum of the simulation result.

the axle box. The test is carried out under four conditions with the same radial load of 146 kN and different rotational speeds, i.e., 589 RPM, 786 RPM, 983 RPM. The sampling frequency for all tests is set to 20 kHz. The experimental setup is shown in Fig. 7.

The parameters of the bearings used in the two experiments are shown in Table 2.

#### 4.2. Basic model performance analysis

The acceleration signals obtained by experiment and simulation are shown in Fig. 8.

Experimental data from the CWRU dataset at the end of the fan with a defect size of 0.1778 mm and operating conditions of 1 HP/1772 RPM are used as a reference. It should be noted that it is difficult to obtain significant fault frequency domain features using the raw data of ball faults in the CWRU dataset directly. Therefore, signal processing is usually required to amplify the fault frequency components.

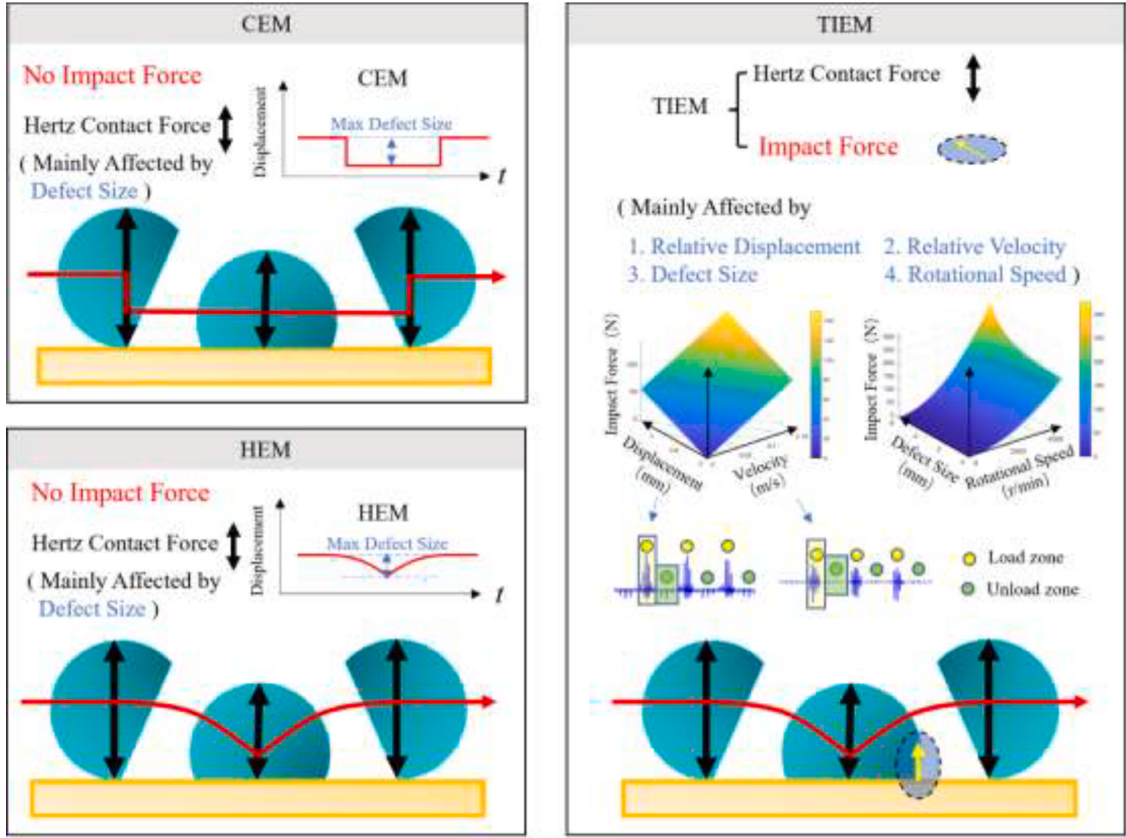


**Fig. 9.** The characteristics and comparison of the three models.

The envelope spectrum of the original signal is shown in Fig. 10(b)(d)(f), and the smaller sized image in the upper right corner shows the frequency characteristics of the system from 0 to 6000 Hz. It can be seen that the system of CWRU resonates significantly in all the 0–4000 Hz band. Even the fault components in the low frequency range of 0–500 Hz are heavily affected by the frequency of rotation ( $f_r$ ). In order to extract the clear fault components, the original signal is signalized using a three-layer wavelet packet transform. The filtered signal using its third layer at the fifth node is reconstructed to obtain the waveform and frequency domain features shown in Fig. 10(c)(d).

In every revolution the rolling element strikes both inner and outer races. Thus, the rolling element fault frequency ( $f_{RE}$ ) is supposed to be twice the ball/ rolling element spinning frequency, which is shown in Eq. (28):

$$f_{RE} = \frac{D}{d} \left[ 1 - \left( \frac{d}{D} \cos \alpha \right)^2 \right] f_r \quad (28)$$

As shown in Fig. 10(b), the amplitude of  $f_{RE}$  in the unprocessed experimental signal is small, and the characteristics are not obvious. As shown in Fig. 10(d), the fault frequency characteristic is the most obvious in reconstructed signals. The influence of rotational frequency is reduced, and the multiple components of the fault frequency are derived. As shown in Fig. 10(e), there are clear pulse components in the acceleration signal obtained through the proposed fault model simulation. The time interval of the fault shock pulse is 0.0085 s, and the cage rotation period is 0.09 s. Simultaneously, the difference between the amplitude of the experimental results obtained from the simulation and the real data is not significant, indicating that the proposed model has good mechanical properties. The envelope analysis of the waveform is performed, and the envelope spectrum shown in Fig. 10(f) is obtained. Among them, the rolling element fault frequency and multiplier components are modulated by the cage fault frequency ( $f_c$ ), which is also consistent with the typical characteristics of the bearing with rolling element defects. Experimental results show that the proposed dynamic model can be used to study the bearing rolling element fault.

Since the amplitude levels of the actual experimental data and the model simulation results are different, a comparison experiment is set up in this paper to verify the performance of the proposed model. Two conventional dynamic models are used for comparison: constant displacement excitation function model (CEM) [18] and half-sine excitation function model (HEM) [20].

Fig. 9 shows the difference between the three models. The main characteristics of them are as follows:

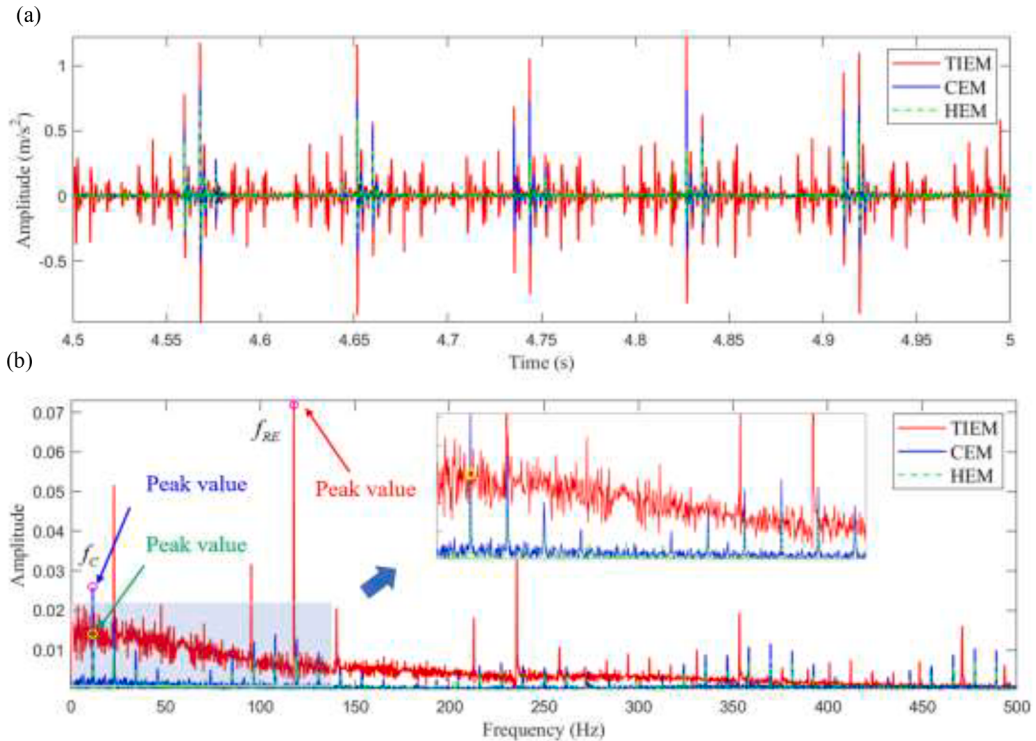


**Fig. 10.** Vibration signal comparison results of three models. (a) Time domain signal of the simulation results, and (b) envelope spectrum (the envelope signal is obtained based on Hilbert transform) of the simulation results.

- 1 CEM: assumes that the rolling unit directly reaches the maximum value of displacement once it enters the spall region, and regains contact instantly when exiting from that area.
- 2 HEM: assumes that the displacement of the rolling unit in the defect area conforms to the law of sine function, which can reflect the overall trend of the displacement of the rolling element from entering the defect area to exiting the defect area, and is more widely used.
- 3 TIEM: The time-varying impact excitation function model (TIEM), which is proposed in this paper.

Fig. 10 shows the simulated signal comparison between the three models. It can be seen that TIEM makes the energy and impact of the rolling element fault frequency component more significant by using the impact force function. The peak value of the TIEM model is concentrated near the characteristic frequency component of the bearing rolling element. In contrast, the cage fault frequency component plays a dominant role and has a high peak value in CEM and HEM. This result indicates that the impact force strengthens the role of the bearing rolling element. The proposed TIEM model enhances the signal pulse amplitude and enriches the complexity of the time domain signal compared with the two-other dynamics model. It strengthens the rolling element fault frequency component in the frequency domain to make the model vibration intensity greater under the same physical parameters. The TIEM model is easier to identify the fault frequency of the rolling elements, which has stronger similarity to the data collected under the working conditions with obvious faulty impact and overcomes the problem that the conventional model is dominated by the cage fault frequency component.

The simulation of the conventional dynamics model requires high-quality model parameters because of its poor generalization ability. The conventional dynamics model will lose its fault characteristics after replacing some physical parameters. Therefore, it is necessary to recalculate mechanical parameters, such as bearing contact stiffness. The same set of parameters may lead to a decrease in model performance. The time domain and frequency domain simulation waveforms of the three models with different defect sizes are shown in Fig. 11. The amplitude of the frequency domain data at 0.3556 mm is much larger than that at 0.1778 mm. Hence the frequency domain data in Fig. 11 are normalized to allow for a clearer representation of the peak value.

Without adjusting the parameters when the defect size has been changed, the two conventional models show serious performance degradation when the rolling element defect size is 0.1778 mm, as schematically shown in Fig. 11. The peak of the envelope spectrum has shifted from the fault frequency to other frequency components. And the amplitude at the critical frequency is very low when the defect size is 0.1778 mm. The TIEM model maintains better performance when the parameters are varied. It maintains similar characteristics at both defect sizes, and the key feature frequency amplitudes are clearly reflected. This feature enables the initial verification of the generalization ability of the model.

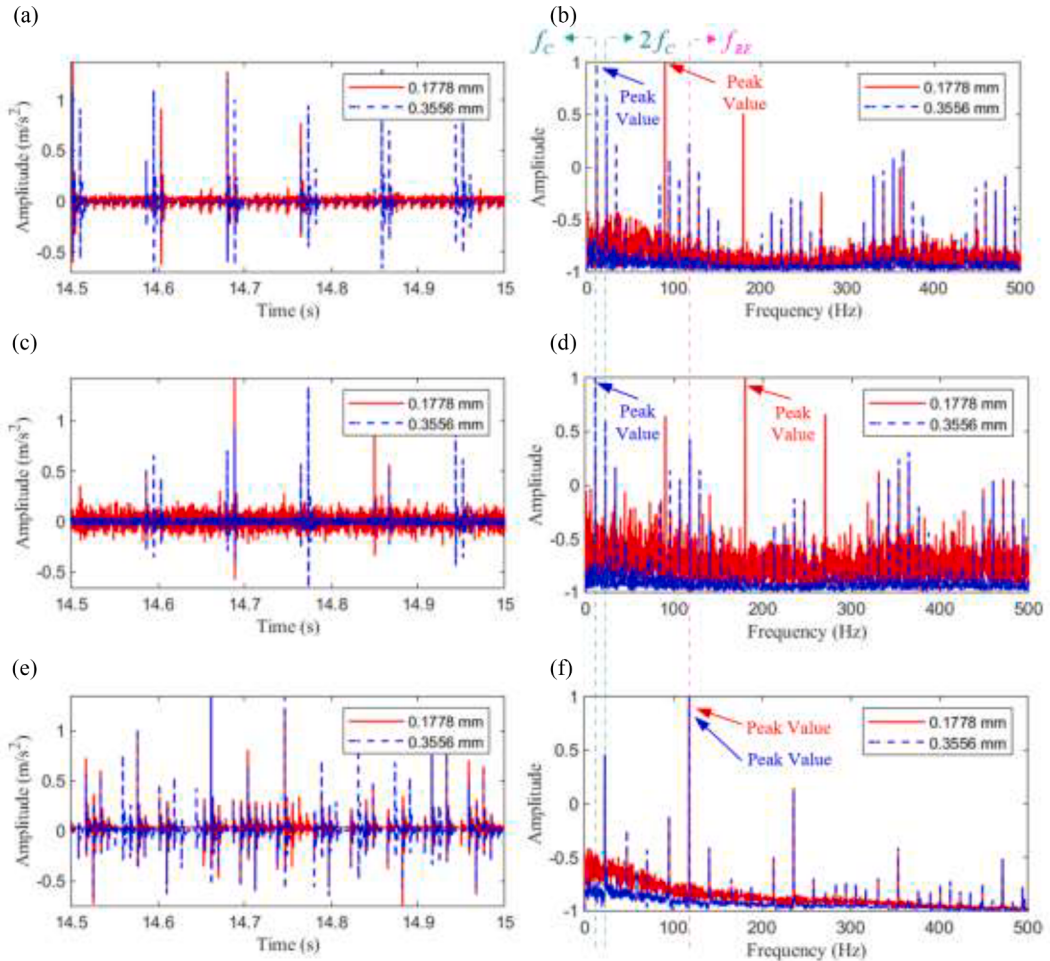


**Fig. 11.** Comparison results of simulation results with different defect sizes. (a) Time domain signal of the CEM model, (b) envelope spectrum (the envelope signal is obtained based on Hilbert transform) of the CEM model, (c) time domain signal of the HEM model, (d) envelope spectrum of the HEM model, (e) time domain signal of the TIEM model, and (f) envelope spectrum of the TIEM model.

#### 4.3. Vibration characteristics of the ball bearing

The size of defects seriously affects the performance of bearings [50]. During the full life cycle of bearings, the phenomenon of increased vibration due to the continuous expansion of the size of the defects is widespread. The size of defects is a very important factor which can affect the vibration characteristics. In this section, three different defect sizes and four different speeds are used to simulate different fault states when the bearing rolling element fails, and the acceleration of simulation and experiment is compared and analyzed.

The influence of defect sizes and speeds on vibration characteristics is discussed by using experimental data. The root mean square (RMS) value of the fan end in CWRU dataset is shown in Fig. 12(a). The RMS value of the experimental data when the defect size is 0.3556 mm is generally higher than that when the defect size is 0.1778 mm. This result indicates that the bearing defect size is monotonously related to the bearing vibration intensity. Nonetheless, its RMS value does not show a strong correlation with the speed signal. Because the speed span from 1730 RPM to 1797 RPM is too small to be representative, it is difficult for this experimental result to directly explain that the RMS value is not related to the speed. This feature will be discussed aimed at the RTSE dataset in the next section.

As can be seen in Fig. 12(a), the RMS values when the defect size is 0.5334 mm are generally smaller than those when the defect size is 0.3556 mm. This result is clearly not in accordance with the general rule. The CWRU data set was thoroughly investigated in Ref. [49]. The fault frequency components of the four data sets with a defect size of 0.5334 mm could barely be identified during signal processing and were questioned to be problematic. Therefore, there is a high probability that the experiment for this condition has a large error, leading to the inconsistency shown in Fig. 14(a).

Fig. 12(b)(c)(d) show the RMS values of the vibration simulation results of these models. Inconsistent with the experimental results, the RMS values of the simulated signals at 0.5334 mm are generally higher than those at 0.3556 mm. To show the performance of each

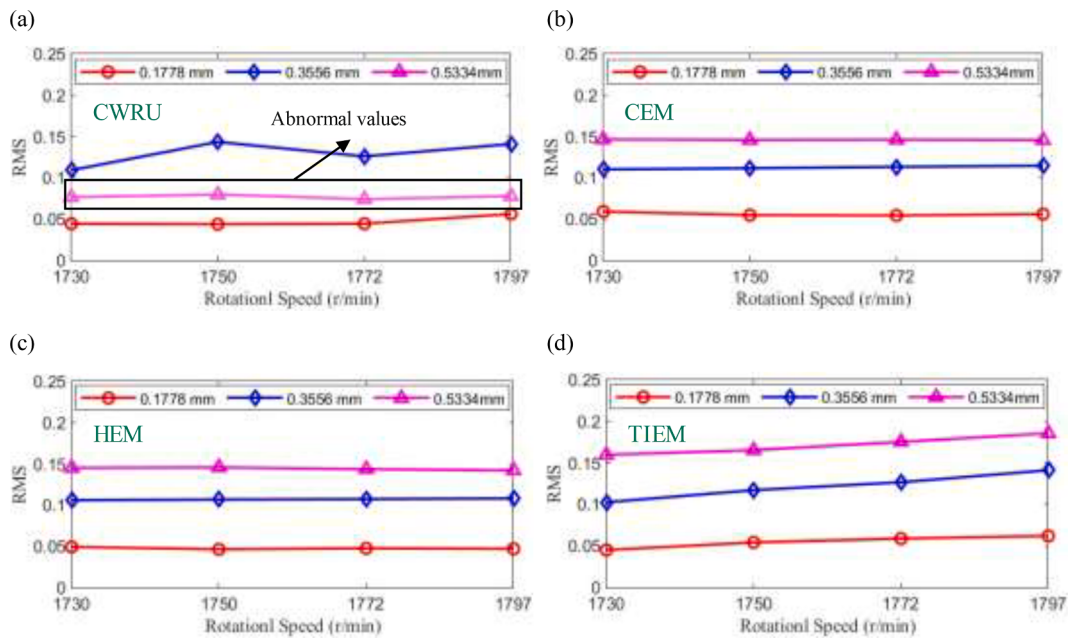


**Fig. 12.** RMS of experimental vibration acceleration and simulation vibration acceleration under different bearing defect sizes and speeds. (a) RMS of experimental signal, (b) RMS of the CEM model, (c) RMS of the HEM model, (d) RMS of the TIEM model.

**Table 3**  
RMS values of experiments and individual models.

RMS of experiment-CWRU ( $\text{m/s}^2$ )				RMS of CEM ( $\text{m/s}^2$ )					
	1730 RPM	1750 RPM	1772 RPM	1797 RPM		1730 RPM	1750 RPM	1772 RPM	1797 RPM
0.1778mm	0.0445	0.0440	0.0446	0.0564	0.1778mm	0.0593	0.0550	0.0546	0.0562
0.3556mm	0.1062	0.1435	0.1260	0.1410	0.3556mm	0.1103	0.1117	0.1133	0.1147
0.5334mm	0.0767	0.0800	0.0743	0.0780	0.5334mm	0.1466	0.1459	0.1462	0.1458
RMS of HEM ( $\text{m/s}^2$ )				RMS of TIEM ( $\text{m/s}^2$ )					
	1730 RPM	1750 RPM	1772 RPM	1797 RPM		1730 RPM	1750 RPM	1772 RPM	1797 RPM
0.1778mm	0.0496	0.0467	0.0479	0.0473	0.1778mm	0.0452	0.0543	0.0589	0.0622
0.3556mm	0.1062	0.1070	0.1075	0.1083	0.3556mm	0.1026	0.1172	0.1267	0.1412
0.5334mm	0.1453	0.1459	0.1437	0.1423	0.5334mm	0.1597	0.1653	0.1753	0.1856

model more clearly, the RMS values of each model under various conditions are listed in [Table 3](#). The comparison shows that in addition to the more pronounced vibration of the TIEM model at the defect size of 0.5334 mm, TIEM is also very sensitive to the rotational speed. Besides, simulation data generated by TIEM has better monotonicity at each defect size.

#### 4.4. Vibration characteristics of the roller bearing

Rotational speed is a crucial physical parameter in the operation of bearings. The test rig of CWRU does not directly adjust the motor speed, which makes it difficult to discover the influence of rotational speed on vibration characteristics in its data characteristics. At the same time, there is no external load in the CWRU experiment. It is necessary to further verify the vibration characteristics of the model under external load. Therefore, supplementary experiment of rotational speed is carried out in this section. The parameters of the bearings used in the supplementary experiment are shown in [Table 2](#).

The force characteristics of the defective rolling elements during the contact process are shown in [Fig. 13\(a\)\(b\)](#). It can be seen that in the TIEM model, the magnitude of the Hertz contact force generated by the extrusion is larger than the impact force. The Hertz contact force disappears after the rollers exit the load zone. Due to the presence of the impact force, tiny pulses will still be generated in the unload zone. In [Fig. 13\(c\)](#), two distinct impacts (label as pink and yellow) occur at the moment when the defect of the rolling element starts to contact and exit the contact state, and the double-impact phenomenon has also been widely discussed and used in previous studies [25]. Through the calculation of the impact force generated by the defect displacement, the duration of the impact force  $F_{im1}$  is less than 1 ms, and the trend is similar to the inverse sine function which has time-varying characteristics. The external load causes the inner and outer races to extrude the rolling elements to produce a relative offset, and the impact force  $F_{im2}$  generated by the offset is in the form of an oscillating pulse, as shown in [Fig. 13\(d\)](#).

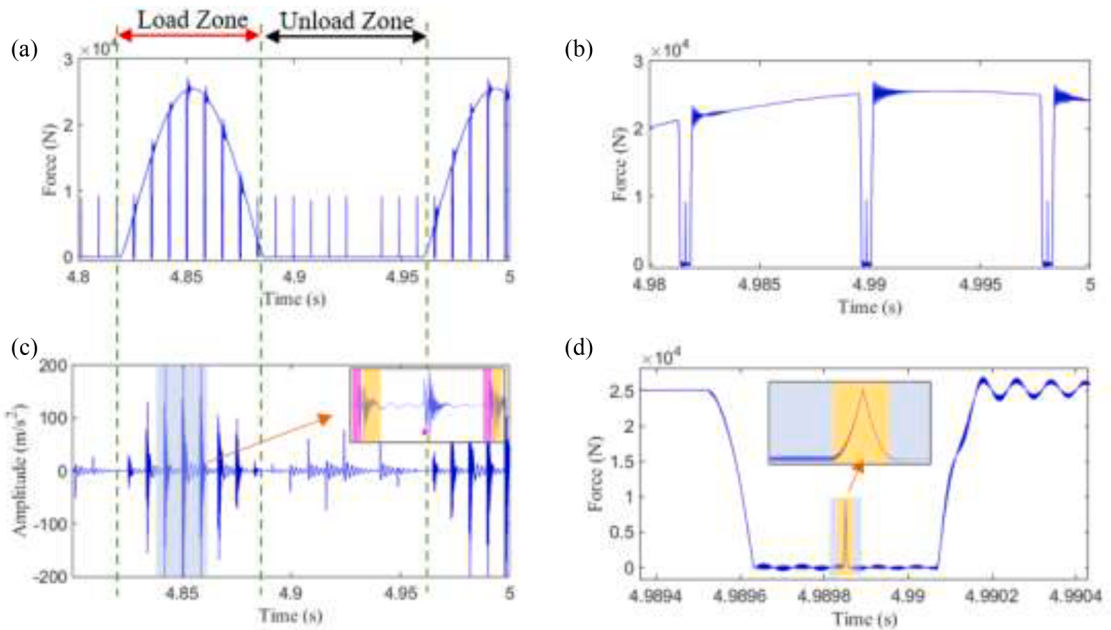


**Fig. 13.** The force and vibration waveform of the defective rolling element (a) The force of the defective rolling element in one rotation cycle (b) The partial amplification of the force waveform (c) The vibration waveform in one rotation cycle (d) Local amplification of the impact force at the center of the load.

The physical parameters used in the experiment are input into the proposed model to generate vibration signals at different rotational speeds as shown in Fig. 14.

The characteristic frequency of the rolling element fault and the side-frequency characteristics of the cage fault frequency can be clearly seen in the simulated signal. The simulation results are consistent with the experiment results under different working conditions. With the increase of rotational speed, the impact period of time domain signal becomes more and more intensive. At 589/786/983 RPM, there are 4/5/6 obvious impacts in the time domain of experimental and simulated signals, respectively. In frequency domain, there are multiple frequency spikes with a numerical magnitude equal to the multiple of  $f_{RE}$ . Although the cage fault frequency  $f_c$  is still present, it is almost always lower than  $f_{RE}$ . The simulated signal clearly reflects the fault frequency component in the original signal and qualitatively reflects the apparent fault effects in the experimental data. The high similarity of vibration characteristics between the fault enhancement signal of TIEM and the signal of experimental data also shows that the impact force is one of the important factors which should not be ignored in the complex movement process.

The RMS of all working conditions in Fig. 14 are plotted in Fig. 15. With the increase of rotational speed and defect size, the RMS value of vibration signal increases gradually. The RMS amplitude of the simulated signal is highly consistent with that of the experimental data, which quantitatively demonstrates the effectiveness of TIEM. Both ball bearings and roller bearings have the same RMS variation rule, and the amplitude difference between simulation and experiment is very small. The RMS values of the two simulated signals are consistent with the RMS values of the experimental signals, which proves that the proposed model reflects the radial vibration characteristics of the two different bearings simultaneously. To show the performance of TIEM more clearly, the RMS values of experiments (RTSE) and TIEM under various conditions are listed in Table 4.

## 5. Conclusion

In this paper, a dynamic model TIEM considering time-varying excitation is proposed. The accuracy and strong generalization capability of the proposed model are verified by the experimental data. The following specific conclusions can be obtained:

- (1) An impact force function with time-varying characteristics is proposed, which is directly related to rotational speeds and defect sizes. The four-degree-of-freedom dynamic model with this force can accurately reflect the vibration characteristics of bearings with local rolling element defects.
- (2) TIEM has typical time domain characteristics and frequency domain characteristics. The influence of the cage and rolling element fault components is ensured in both the time and frequency domains. A series of strong shocks occur during the cage rotation in the time domain, including the double shock phenomenon. In the frequency domain, the fault frequency of the rolling elements and the cage fault frequency are the most obvious components.
- (3) The simulation results have shown that TIEM has a better generalization capability than conventional models due to the time-varying impact force. TIEM has a significant improvement on the fault frequency component.

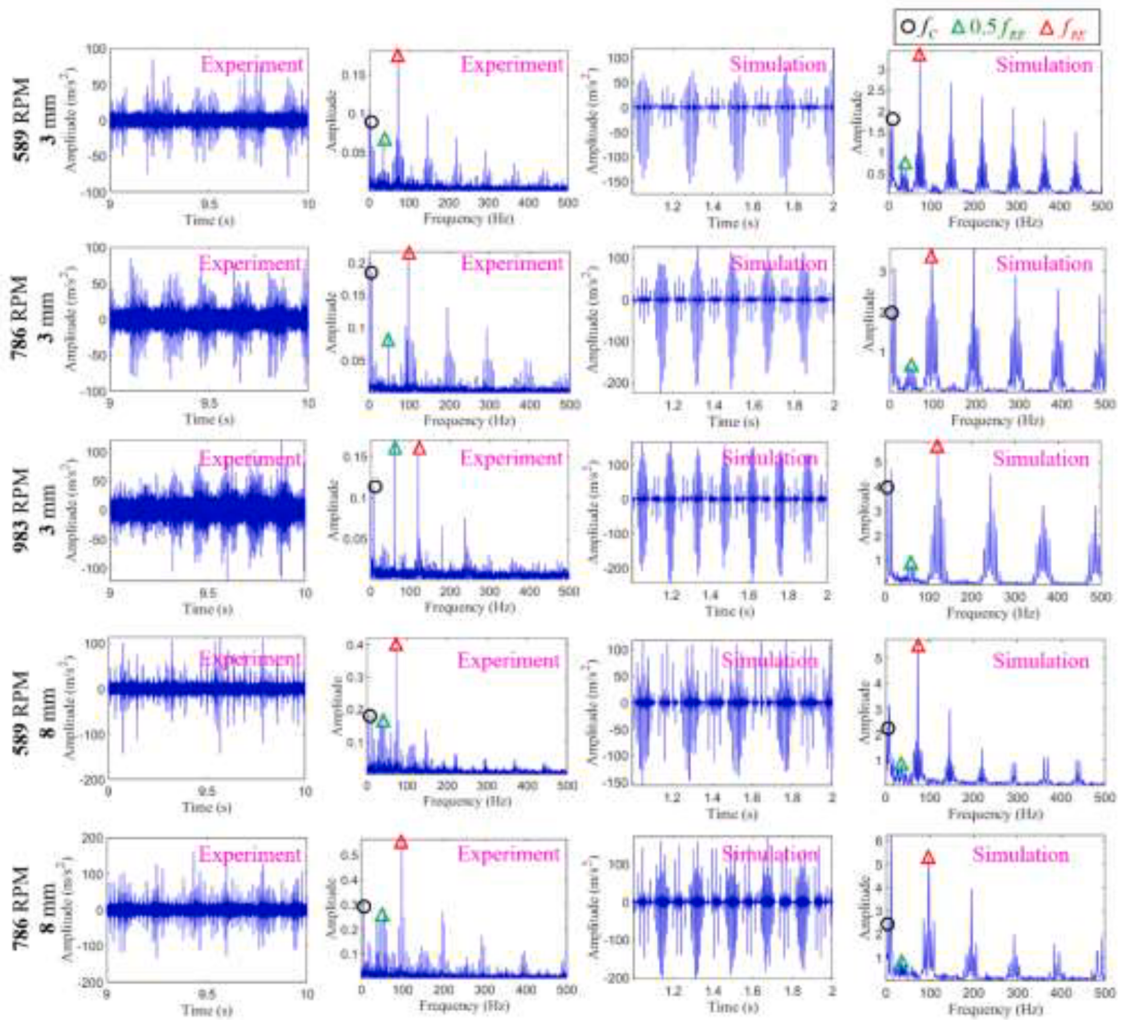


**Fig. 14.** Vibration characteristics of rolling bearings under different rotational speeds and defect sizes.

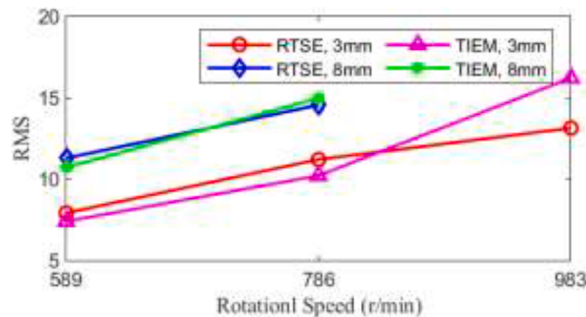


**Fig. 15.** RMS of experimental vibration acceleration and simulation vibration acceleration under different bearing defect sizes and speeds.

(4) Comparison with the experimental data shows that the proposed model can reflect the trend of the actual characteristics. It is concluded that bearing vibration intensity is positively correlated with rotational speeds and defect sizes. Furthermore, the model provides a reference for understanding the mechanism of rolling bearing fault derivation.

**Table 4**

RMS values of experiments and the TIEM model.

RMS of experiment-RTSE ( $\text{m/s}^2$ )			RMS of TIEM ( $\text{m/s}^2$ )		
	3mm	8mm		3mm	8mm
589 RPM	7.9242	11.2890	589 RPM	7.4079	10.7114
786 RPM	11.2104	14.5535	786 RPM	10.2196	14.9845
983 RPM	13.1381	—	983 RPM	16.2145	—

## Funding

This work was supported by the SKLMT-MSKFKT-202110, the National Natural Science Foundation of China under Grant 52275134, the National Key R&D Program of China under Grant 2022YFB3402100, and the Natural Science Foundation of Sichuan, China under Grant 2023NSFSC1960.

## CRediT authorship contribution statement

**Ruiqi Zhang:** Conceptualization, Methodology, Investigation, Writing – review & editing, Supervision. **Liang Guo:** Formal analysis, Writing – original draft, Writing – review & editing, Visualization, Project administration, Funding acquisition. **Zhuyuxiu Zong:** Validation, Data curation, Software. **Hongli Gao:** Supervision, Funding acquisition. **Mengui Qian:** Software. **Zaigang Chen:** Supervision, Funding acquisition.

## Declaration of Competing Interest

The authors declare that they have no known competing financial interests or personal relationships that could have appeared to influence the work reported in this paper.

## Data availability

The authors do not have permission to share data.

## Acknowledgement

This work was supported in part by the National Natural Science Foundation of China under Grant 51905452 and Grant 51775452, and in part by the Local Development Foundation guided by the Central Government 2020ZYD012.

## References

- [1] I. El-Thalji, E. Jantunen, A summary of fault modelling and predictive health monitoring of rolling element bearings, *Mech. Syst. Signal Process.* 60 (2015) 252–272.
- [2] N. Tandon, A. Choudhury, Review of vibration and acoustic measurement methods for the detection of defects in rolling element bearings, *Tribol. Int.* 32 (1999) 469–480.
- [3] M.S. Patil, J. Mathew, P.K.R. Kumar, Bearing signature analysis as a medium for fault detection: a review, *J. Tribol.* 130 (2008) 1–7.
- [4] M.H. Jalali, M. Ghayour, S. Ziae Rad, B. Shahriari, Dynamic analysis of a high speed rotor-bearing system, *Measurement* 53 (2014) 1–9.
- [5] Y. Lei, N. Li, L. Guo, N. Li, T. Yan, J. Lin, Machinery health prognostics: a systematic review from data acquisition to RUL prediction, *Mech. Syst. Signal Process.* 104 (2018) 799–834.
- [6] D. Wang, K.L. Tsui, Q. Miao, Prognostics and Health Management: a Review of Vibration Based Bearing and Gear Health Indicators, *IEEE Access* 6 (99) (2017) 665–676.
- [7] Y. Yu, L. Guo, H. Gao, Y. Liu, T. Feng, Pareto-optimal adaptive loss residual shrinkage network for imbalanced fault diagnostics of machines, *IEEE Trans. Industrial Informatics* 18 (4) (2022) 2233–2243.
- [8] L. Guo, Y. Lei, N. Li, T. Yan, N. Li, Machinery health indicator construction based on convolutional neural networks considering trend burr, *Neurocomputing* 292 (2018) 142–150.
- [9] Y. Wang, G. Xu, A. Luo, L. Liang, K. Jiang, An online tacholess order tracking technique based on generalized demodulation for rolling bearing fault detection, *J. Sound Vib.* 367 (2016) 233–249.
- [10] Y. Lei, J. Lin, M.J. Zuo, Z. He, Condition monitoring and fault diagnosis of planetary gearboxes: a review, *Measurement* 48 (1) (2014) 292–305.
- [11] Y. Yu, L. Guo, Y. Tan, H. Gao, J. Zhang, Multisource partial transfer network for machinery fault diagnostics, *IEEE Trans. Industrial Electronics* 69 (10) (2022) 10585–10594.
- [12] Z. Liu, Y. Lei, H. Liu, X. Yang, W. Song, A phenomenological model for investigating unequal planet load sharing in epicyclic gearboxes, *Mech. Syst. Signal Process.* 135 (2020), 106414.
- [13] P.D. McFadden, J.D. Smith, Model for the vibration produced by a single point defect in a rolling element bearing, *J. Sound Vib.* 96 (1) (1984) 69–82.
- [14] P.D. McFadden, J.D. Smith, The vibration produced by multiple point defects in a rolling element bearing, *J. Sound Vib.* 98 (2) (1985) 263–273.
- [15] J. Antoni, R.B. Randall, Differential diagnosis of gear and bearing faults, *J. Vib. Acoust.* 124 (2002) 165–171.
- [16] J. Antoni, R.B. Randall, A stochastic model for simulation and diagnostics of rolling element bearings with localized faults, *J. Vib. Acoust.* 125 (3) (2003) 282–289.
- [17] N. Tandon, A. Choudhury, An analytical model for the prediction of the vibration response of rolling element bearings due to a localized defect, *J. Sound Vib.* 205 (3) (1997) 275–292.

- [18] N.S. Feng, E.J. Hahn, R.B. Randall, Using transient analysis software to simulate vibration signals due to rolling element bearing defects, 10 (2002).
- [19] N. Sawalhi, R.B. Randall, Simulating gear and bearing interactions in the presence of faults. Part II: simulation of the vibrations produced by extended bearing faults, *Mech. Syst. Signal Process.* 22 (2008) 1952–1966.
- [20] N. Sawalhi, R.B. Randall, Simulating gear and bearing interactions in the presence of faults. Part I. The combined gear bearing dynamic model and the simulation of localised bearing faults, *Mech. Syst. Signal Process.* 22 (8) (2008) 1924–1951.
- [21] D. Petersen, C. Howard, N. Sawalhi, A. Moazen Ahmadi, S. Singh, Analysis of bearing stiffness variations, contact forces and vibrations in radially loaded double row rolling element bearings with raceway defects, *Mech. Syst. Signal Process.* 50–51 (2015) 139–160.
- [22] L. Niu, H. Cao, Z. He, Y. Li, Dynamic modeling and vibration response simulation for high speed rolling ball bearings with localized surface defects in raceways, *J. Manuf. Sci. Eng.* 136 (4) (2014) 152–161.
- [23] J. Liu, Y. Shao, T.C. Lim, Vibration analysis of ball bearings with a localized defect applying piecewise response function, *Mech. Mach. Theory* 56 (1) (2012) 156–169.
- [24] P.G. Kulkarni, A.D. Sahasrabudhe, A dynamic model of ball bearing for simulating localized defects on outer race using cubic hermite spline, *J. Mech. Sci. Technol.* 28 (9) (2014) 3433–3442.
- [25] Y. Jiang, W. Huang, J. Luo, W. Wang, An improved dynamic model of defective bearings considering the three-dimensional geometric relationship between the rolling element and defect area, *Mech. Syst. Signal Process.* 129 (2019) 694–716.
- [26] Y. Liu, Z. Chen, L. Tang, W. Zhai, Skidding dynamic performance of rolling bearing with cage flexibility under accelerating conditions, *Mech. Syst. Signal Process.* 150 (2021), 107257.
- [27] J. Liu, Y. Shao, W.D. Zhu, A new model for the relationship between vibration characteristics caused by the time-varying contact stiffness of a deep groove ball bearing and defect sizes, *J. Tribol.* 137 (2015) 1–15.
- [28] J. Liu, Y. Shao, A new dynamic model for vibration analysis of a ball bearing due to a localized surface defect considering edge topographies, *Nonlinear Dyn.* 79 (2) (2015) 1329–1351.
- [29] J. Liu, Y. Xu, G. Pan, A combined acoustic and dynamic model of a defective ball bearing, *J. Sound Vib.* 501 (1) (2021), 116029.
- [30] D.S. Shah, V.N. Patel, A dynamic model for vibration studies of dry and lubricated deep groove ball bearings considering local defects on races, *Measurement* (2019).
- [31] S. Khanam, J.K. Dutt, N. Tandon, Impact force based model for bearing local fault identification, *J. Vib. Acoust.* 137 (5) (2015).
- [32] Q. Liu, G. Yu, Dynamic model of faulty rolling element bearing on double impact phenomenon, in: 2015 IEEE International Conference on Information and Automation, IEEE, 2015.
- [33] S. Sassi, B. Badri, M. Thomas, A numerical model to predict damaged bearing vibrations, *J. Vib. Control* 13 (11) (2007) 1603–1628.
- [34] Z. Kiral, H. Karagüllü, Vibration analysis of rolling element bearings with various defects under the action of an unbalanced force, *Mech. Syst. Signal Process.* 20 (8) (2006) 1967–1991.
- [35] C. Mishra, A.K. Samantaray, G. Chakraborty, Ball bearing defect models: a study of simulated and experimental fault signatures, *J. Sound Vib.* 400 (2017) 86–112.
- [36] M. Cao, J. Xiao, A comprehensive dynamic model of double-row spherical roller bearing-Model development and case studies on surface defects, preloads, and radial clearance, *Mech. Syst. Signal Process.* 22 (2) (2008) 467–489.
- [37] A. Choudhury, N. Tandon, Vibration response of rolling element bearings in a rotor bearing system to a local defect under radial load, *J. Tribol.* 128 (2) (2006) 252–261.
- [38] H. Arslan, N. Aktürk, An investigation of rolling element vibrations caused by local defects, *J. Tribol.* 130 (2008) 1–12.
- [39] A. Rafsanjani, S. Abbasion, A. Farshidianfar, H. Moeenfar, Nonlinear dynamic modeling of surface defects in rolling element bearing systems, *J. Sound Vib.* 319 (3–5) (2009) 1150–1174.
- [40] P.K. Gupta, Advanced Dynamics of Rolling Elements, Springer-Verlag, New York, 1984.
- [41] P.K. Gupta, Dynamics of rolling-element bearings part III: ball bearing analysis, *J. Tribol.* 101 (3) (1979) 312–318.
- [42] H. Cao, S. Su, X. Jing, D. Li, Vibration mechanism analysis for cylindrical roller bearings with single/multi defects and compound faults, *Mech. Syst. Signal Process.* 144 (2020), 106903.
- [43] L. Niu, H. Cao, H. Hou, B. Wu, Y. Lan, X. Xiong, Experimental observations and dynamic modeling of vibration characteristics of a cylindrical roller bearing with roller defects, *Mech. Syst. Signal Process.* 138 (2020), 106553.
- [44] A. Palmgren, Ball and Roller Bearing Engineering, SKF Industries, Inc., Philadelphia, (n.d.).
- [45] J. Sopanen, A. Mikkola, Dynamic model of a deep-groove ball bearing including localized and distributed defects. Part 1: theory, *Proceedings of the Institution of Mechan. Eng., Part K: J. Multi.Body Dyn.* 217 (2003) 201–211.
- [46] W. Zhang, Y. Liu, Y. Liao, P. Liu, The dynamic analysis of a freight train rolling bearing with outer ring fault, in: ICRT 2017: Railway Development, Operations, and Maintenance - Proceedings of the 1st International Conference on Rail Transportation 2017, 2018, pp. 901–911.
- [47] T.A. Harris, Essential concepts of bearing, Technology (Singap World Sci) (2008).
- [48] Case Western Reserve University Bearing Data Center Website (<http://csegroups.case.edu/bearingdatacenter/home>).
- [49] W.A. Smith, R.B. Randall, Rolling element bearing diagnostics using the Case Western Reserve University data: a benchmark study, *Mech. Syst. Signal Process.* 64 (2015) 100–131.
- [50] A. Rohani Bastami, S. Vahid, A comprehensive evaluation of the effect of defect size in rolling element bearings on the statistical features of the vibration signal, *Mech. Syst. Signal Process.* 151 (2) (2021), 107334.